Microstructural evolution of Si(Hf_xTa_{1-x})(C)N polymer-derived ceramics upon high-temperature anneal

Nathalie Thor [a,*], Jan Bernauer [b], Nils-Christian Petry [c], Emanuel Ionescu [b,e], Ralf Riedel [b], Astrid Pundt [d], Hans-Joachim Kleebe [a]

[a] *Technical University Darmstadt, Institute of Applied Geoscience, Schnittspahnstraße 9, D-64287 Darmstadt, Germany*
[b] *Technical University Darmstadt, Institute of Materials Science, Otto-Berndt-Straße 3, D-64287 Darmstadt, Germany*
[c] *DECHEMA Research Institute, Materials and Corrosion, Theodor-Heuss-Allee 25, D-60486 Frankfurt am Main, Germany*
[d] *Karlsruhe Institute of Technology, Institute for Applied Materials – Materials Science and Engineering (IAM-WK), Engelbert-Arnold-Straße 4, D-76131 Karlsruhe, Germany*
[e] *Fraunhofer Research Institution for Materials Recycling and Resource Strategies (IWKS), Brentanostraße 2a, D-63755 Alzenau, Germany*

Keywords:
Polymer-derived ceramic
Electron microscopy, thermal decomposition
UHTC
Transition metal carbide

ABSTRACT

Ultra-high temperature ceramic nanocomposites (UHTC-NC) within the Si(Hf_xTa_{1-x})(C)N system were synthesized via the polymer-derived ceramics (PDC) synthesis route. The microstructure evolution of the materials was investigated upon pyrolysis and subsequent heat treatment. The crystallization behavior and phase composition were studied utilizing X-ray diffraction, scanning- and transmission electron microscopy. Single-source-precursors were converted into amorphous single-phase ceramics, with the exception of surface crystallization effects, at 1000 °C in NH_3. Annealing in N_2 at 1600 °C resulted in fully crystalline UHTCs. The powder samples revealed microstructures consisting of two characteristic regions, bulk and surface; displaying intrinsic microstructure and phase composition differences. Instead of the expected nitrides, transition metal carbides (TMC) were detected upon high-temperature anneal. The residual carbon available in the system triggered a decomposition reaction, resulting in the formation of TMCs plus gaseous nitrogen and SiC. Experimental data underline that N-containing PDCs are prone to phase separation accompanied by thermal decomposition and diffusion-controlled coarsening.

1. Introduction

Ultra-high temperature ceramics (UHTCs) have gained renewed attention in the last decades due to their potential use as protective coatings on metal substrates in extreme environments [1–5]. By definition, UHTCs are ceramic materials with melting points above 3000 °C [6,7]. Therefore, they are suitable candidates for thermal protection structures in gas-turbine engines or chemical plants, which can withstand application temperatures exceeding ~1600 °C and aggressive environmental conditions [1,8–11]. In addition to their high melting point, UHTCs combine improved structural properties such as high hardness, excellent chemical stability, high Youngs modulus, high refractoriness, as well as high thermal and electrical conductivity [1,8–10,12]. UHTCs are typically binary compounds consisting of carbides, borides or nitrides of early transition metals (e.g. ZrB_2, HfN, HfC or TaC) [7,8,12]. HfC and its solid solutions with TaC such as ($Hf_{0.2}Ta_{0.8}$)C are advanced structural ceramics, possessing the highest ever known melting points ($T_m = 3940$ °C) among all known refractory materials [7,9,13,14].

Despite their advantages, pure UHTCs lack of a sufficient oxidation resistance, limiting their practical applications [7,8,15]. To improve this property, silica-formers such as SiC, Si_3N_4 or silicides are used as additives, as they form a silica-rich surface layer, which is protective up to at least 1700 °C [1,7,8,16–19]. A preparative route to achieve Si-based oxidation-resistant UHTCs has been followed via the polymer-to-ceramic route, which allows the development of multielement polymer-derived ceramics (PDCs) [20–22]. In this preparative approach, metal-modified ceramic precursors are used to obtain tailored compositions and architectures for the so-called polymer-derived ceramic nanocomposites (PDC-NCs) [8,21]. In general, the synthesis of PDC-NCs can be rationalized as following: the crosslinked polymeric precursor is thermally converted into an amorphous single-phase

---

* Corresponding author.
E-mail address: nathalie.thor@tu-darmstadt.de (N. Thor).

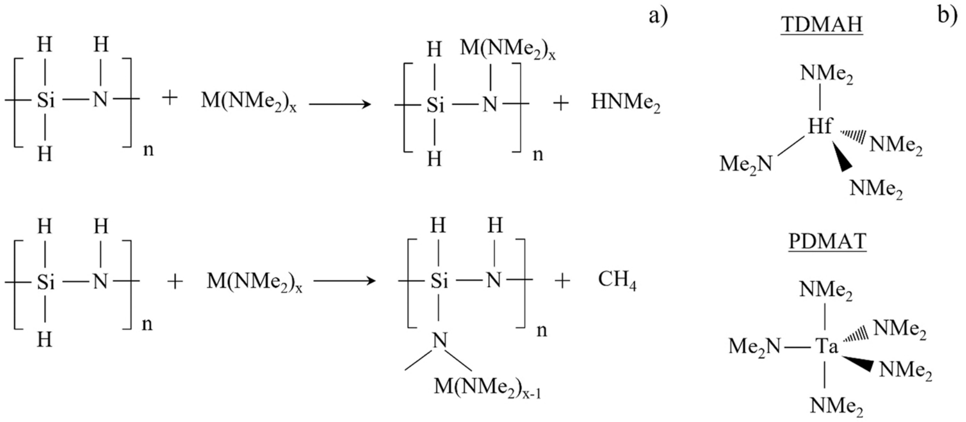

Fig. 1. a) Possible reaction pathways during the synthesis of the single-source precursor between the polymer (PHPS) and the organo-metallic complex ($M(NMe_2)_x$), with M Hf, Ta and Me CH_3; b) structural chemical formular of the organo-metallic dimethylamido complexes of hafnium (TDMAH) and tantalum (PDMAT).

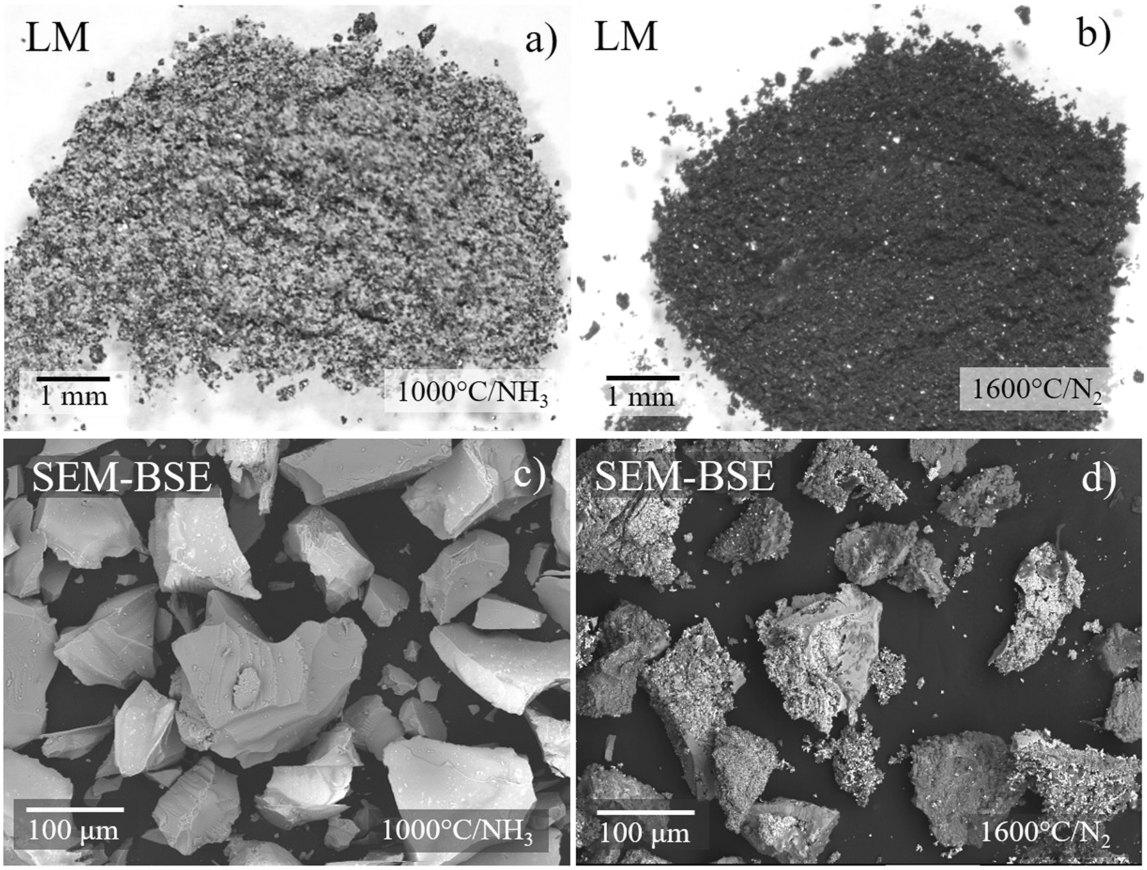

Fig. 2. Optical light microscope (LM) (a,b) and SEM-BSE (c,d) images of the as-pyrolyzed (1000 °C) and annealed (1600 °C) $Si(Hf_{0.2}Ta_{0.8})(C)N$ powder sample.

ceramic at temperatures between 300 °C and 1000 °C, followed by a heat-treatment at higher temperatures (<1500 °C), which induces phase separation and crystallization processes [23,24].

Extensive research was carried out to develop new oxidation-resistant Si-based matrix phases with dispersed nanosized secondary phases containing Hf, Ta and their solid solutions [3,7,25–32]. For the potential application as a protective coating on metal alloys, the PDC route is in particular beneficial, because it allows the preparation of thermal or environmental barrier coatings (TBC, EBC) due to the usage of several inexpensive liquid-phase deposition techniques such as dip-, spray-, and spin coating [1,5,33,34].

As shown in earlier studies, the solid-state microstructure and phase composition of PDCs strongly influence their high-temperature properties [20,35–38]. Moreover, microstructural changes were observed in SiHfCO-based PDCs in surface-near regions (100–200 nm) and inner surfaces (local cracks), as compared to the bulk, in particular, when annealed at higher temperatures [39,40]. These microstructural variations were induced by local changes in chemical composition, affecting diffusional processes and, in turn, the pronounced growth of HfO_2 precipitates close to the sample surface [39,40]. In addition to research on the silicon oxycarbide (Si-O-C) and silicon carbonitride (Si-C-N) systems, Zhou et al. [25] incorporated Hf into a Si-N matrix at the molecular level. Therefore, a novel metal-modified nanocomposite ceramic was designed by the single-source precursor route, utilizing a

Table 1
Synthesis parameter of the Si(Hf_xTa_{1-x})(C)N-based powder samples analyzed in this study.

Sample	TDMAH, PDMAT (metal:metal) molar ratio	TDMAH+PDMAT :PHPS (metal:polymer) molar ratio	Processing temperature in [°C]	Exposure time in [h]	Gas atmosphere
Si($Ta_{0.8}Hf_{0.2}$)(C)N	4:1	3:7	1000	3	NH_3
Si($Ta_{0.8}Hf_{0.2}$)(C)N	4:1	3:7	1600	3	N_2
Si($Hf_{0.7}Ta_{0.3}$)(C)N	7:3	3:7	1000	3	NH_3
Si($Hf_{0.7}Ta_{0.3}$)(C)N	7:3	3:7	1600	3	N_2

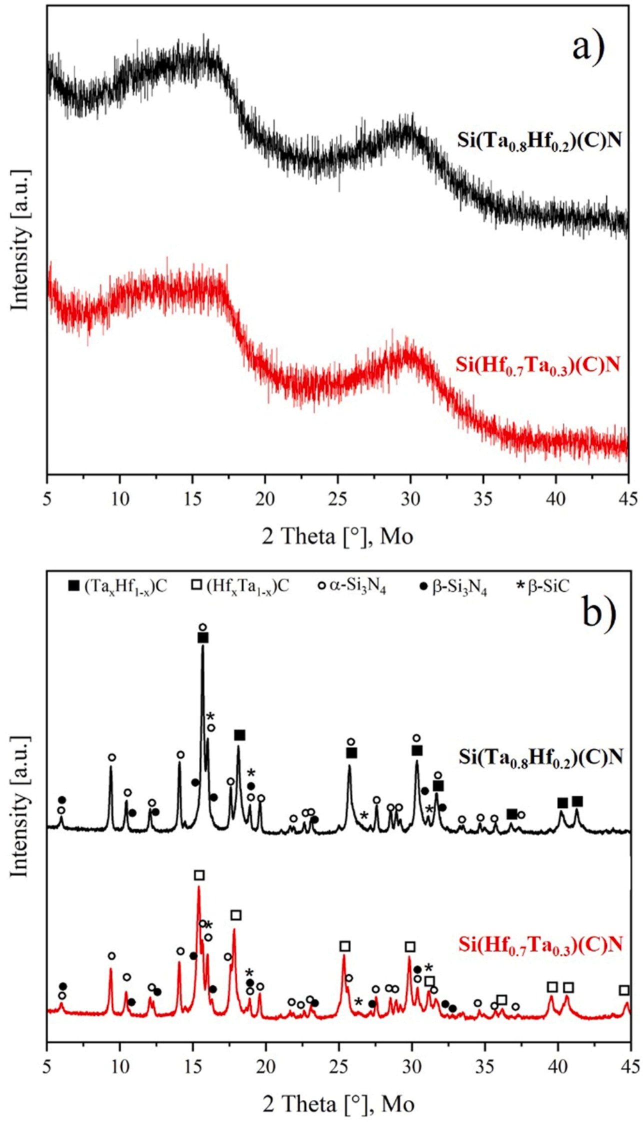

Fig. 3. X-ray powder diffraction (XRD) pattern of Si($Ta_{0.8}Hf_{0.2}$)(C)N (top) and Si($Hf_{0.7}Ta_{0.3}$)(C)N (bottom) polymer derived ceramics showing the structural evolution after the thermal treatment; a) as-pyrolyzed at 1000 °C in NH_3 atmosphere; b) annealed at 1600 °C in N_2 atmosphere.

commercial available perhydropolysilazane (PHPS) upon reaction with a hafnium-modified precursor (tetrakis-(dimethylamido)hafnium(IV) = TDMAH) to achieve simple ternary Si-Hf-N ceramics [25]. Yuan et al. [27] also prepared Hf-based UHTC-NCs, however with small additions of boron and studied their high-temperature oxidation behavior of polymer-derived Si-Hf-B-C-N ceramic nanocomposites [41]. Wen et al. [30] firstly reported on the incorporation of hafnium and tantalum in the Si-C-N system on the atomic scale, forming nanosized solid solutions (Hf_xTa_{1-x})CN embedded in a Si-based matrix phase. Moreover, the synthesis of a metal-modified precursor containing solid solution metal carbide ((Hf_xTa_{1-x})C) remarkably increased the oxidation resistance via a surface passivation treatment prior to oxidation, which generated a silica surface layer [3]. Up to date, only few studies on the high-temperature microstructural characterization of non-oxide Si-based PDC-NCs containing Hf/Ta carbides/nitrides were reported [3,30]. The present study focuses on the microstructural evolution and high-temperature behavior of a novel Si(Hf_xTa_{1-x})(C)N PDC-NC (x = 0.2 and 0.7). The phase composition and microstructural evolution were investigated upon pyrolysis at 1000 °C and compared to the microstructures obtained upon high-temperature anneal at 1600 °C. X-ray powder diffraction (XRD), scanning- (SEM) and transmission electron microscopy (TEM) techniques as well as energy dispersive X-ray spectroscopy (EDS) were employed for detailed structural and chemical characterization.

2. Materials and methods

2.1. Synthesis of Si(Hf_xTa_{1-x})(C)N ceramics

Silicon-based preceramic polymers were used to synthesize PDCs in the Si(M)(C)N (M = metal) system via the polymer-derived ceramics synthesis route. Two polymer-derived ceramic nanocomposites Si(M)(C)N, (M = Hf, Ta), with a Ta:Hf molar ratio of 4:1($Ta_{0.8}Hf_{0.2}$) and a Hf:Ta molar ratio of 7:3 ($Hf_{0.7}Ta_{0.3}$), were prepared via the polymer-to-ceramic transformation upon pyrolysis.

The preparation of the single-source precursor of the Si(Hf_xTa_{1-x})(C)N ceramics with different molar ratios (x = 0.2; x = 0.7) was carried out under purified argon using the standard Schlenk technique. The ratio between the two transition metal compounds is given by x. Both precursors were synthesized by the reaction of the perhydropolysilazane Durazane-2250 (PHPS, 20 wt.-% in di-n-butyl ether, Merck KGaA, Germany) with tetrakis(dimethylamido)hafnium(IV) (TDMAH, 99.99%, Sigma-Aldrich, USA) and pentakis(dimethylamido)tantalum(V) (PDMAT, 99.99%, Sigma-Aldrich, USA) at room temperature. The possible reaction pathways of the synthesis route are given schematically in Fig. 1.

The mass ratio of the transition metal complex to polymer was set to 3:7 (metal complex = TDMAH + PDMAT). The synthesis of Si($Hf_{0.7}Ta_{0.3}$)(C)N is taken as an example to describe the procedure in detail. 11.66 g of PHPS was dissolved in toluene (anhydrous, 99.8%, Sigma-Aldrich, USA) in a 250 ml Schlenk-flask with a magnetic stirrer. Then 0.7 g TDMAH and 0.34 g PDMAT dissolved in 10 ml toluene were added dropwise, and the solution was further stirred for 6 h. The solvent was removed to obtain a yellow-brown powder. This powder was crushed inside the glovebox in a clean agate pestle and mortar. The powder was then sieved, resulting in particle sizes below 100 μm. The powder was subsequently pyrolyzed at 1000 °C in flowing ammonia (NH_3) atmosphere (1 bar) for 3 h to prepare a Si($Hf_{0.7}Ta_{0.3}$)(C)N ceramic powder. The continuous flow of NH_3 was utilized in order to remove the decomposition gases developing during pyrolysis of the system.

Afterwards, annealing of the as-pyrolyzed ceramic powders was performed at 1600 °C in nitrogen (N_2) atmosphere (1 bar) for 3 h, to investigate the resulting microstructure and to detect possible changes

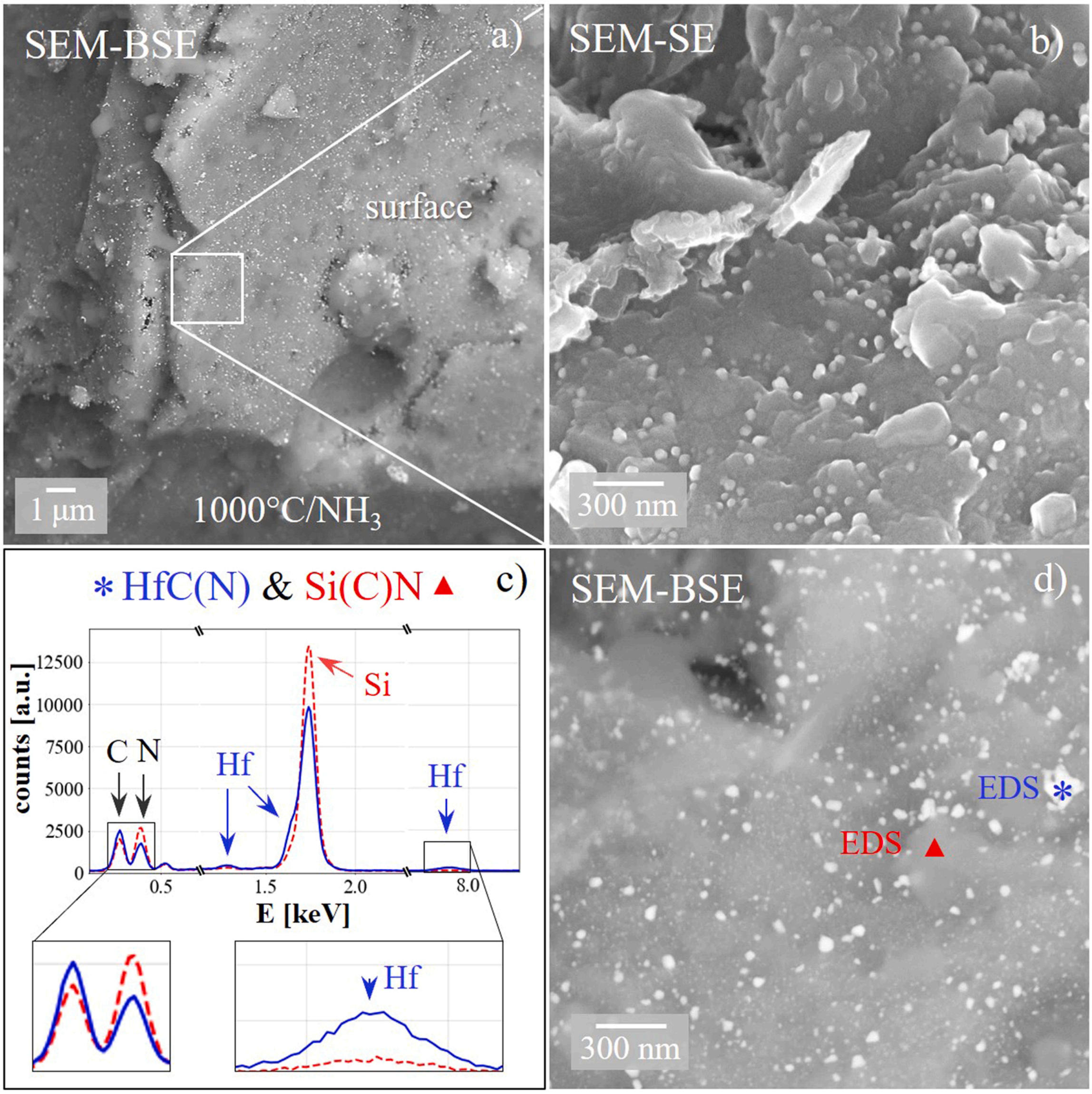

Fig. 4. SEM-BSE (a,d) and -SE (b) micrographs of the $\mathrm{Si(Hf_{0.7}Ta_{0.3})(C)N}$ powder sample pyrolyzed at 1000 °C in NH_3 atmosphere, showing the powder particle surface with nanosized Hf-rich precipitates; c) EDS spectra of a Hf(Ta)C-rich precipitate (continuous blue line) and a second spectrum showing the Si(C)N-rich matrix phase (dashed red line) taken at the location indicated by an asterisk and a triangle symbol, respectively in d).

in the present phase assemblage. Optical light micrographs (LM) and scanning electron microscopy (SEM) backscattered electron (BSE) images in Fig. 2 show the powder samples before and after heat treatment of the synthesized $\mathrm{Si(Hf_{0.2}\,Ta_{0.8})(C)N}$ sample.

All parameters used during the preparation of the as-pyrolyzed and heat-treated materials are given in Table 1, where the corresponding nomenclature of the prepared $\mathrm{Si(Hf_xTa_{1-x})(C)N}$ ceramics is listed.

2.2. *Materials characterization*

The as-pyrolyzed and heat-treated samples were structurally characterized by XRD, SEM, and TEM. XRD was performed on a STOE X-ray diffractometer (STOE & Cie GmbH, Darmstadt, Germany) with a Debye-Scherrer camera equipped with a Mo-Kα radiation source ($\lambda = 0.7093$ Å). The measured 2θ range was 5–45°. Diffraction peaks were indexed using the *Match!* software. Scanning electron microscopy (SEM) was performed on a JSM-7600 F (JEOL Ltd., Tokyo, Japan) coupled with energy-dispersive X-ray spectroscopy (EDS) detector (Oxford Instruments, Abingdon, United Kingdom). Backscattered electron (BSE) and secondary electron (SE) images were taken at an acceleration voltage of 15 kV. EDS point measurements were taken at an acceleration voltage of 15 kV and a working distance (WD) of 8 mm. The beam size diameter was smaller than 2 nm. The acquisition time for each EDS point measurement was 30 s, the estimated relative error ~5%. Transmission electron microscopy (TEM) analysis were performed employing a JEM-2100 F microscope (JEOL Ltd., Tokyo, Japan) operating at an accelerating voltage of 200 kV also equipped with an Oxford EDS detector. In addition, the selected area electron diffraction (SAED) technique was employed to gain crystallographic information and to identify the phase assemblage that formed upon pyrolysis and high-temperature anneal, respectively.

To obtain electron transparency for TEM analysis, ceramic powders were mechanically crushed (pulverized) with a clean agate pestle and mortar in ethanol, followed by ultrasonication also in ethanol and placed on a lacy carbon gold grid.

The pulverized powder was coated with a thin carbon layer to avoid sample charging under the incident electron beam. The use of TEM gold grids was required due to a peak overlap between the L_α lines of the

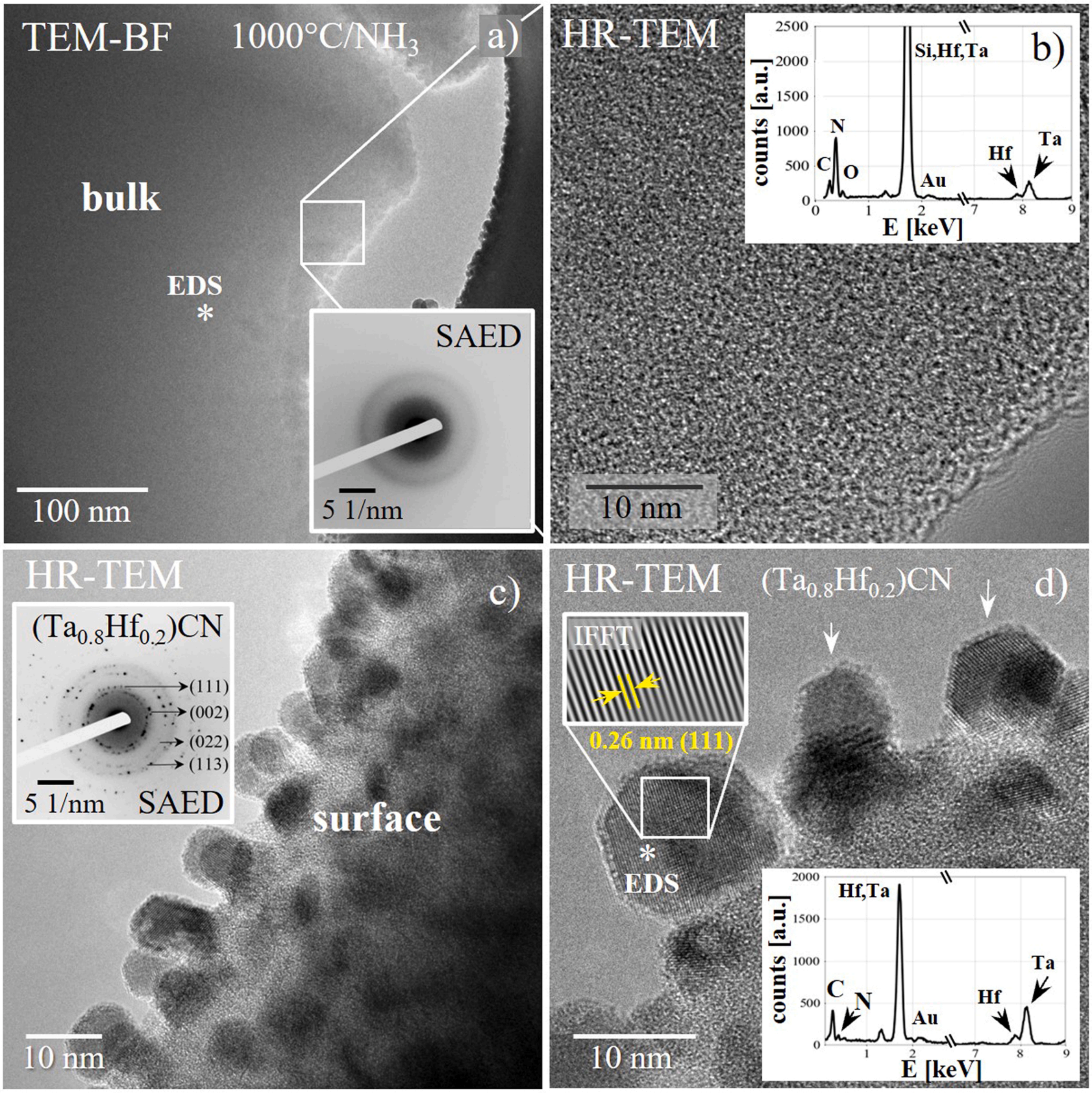

Fig. 5. TEM micrographs of the Si($Ta_{0.8}Hf_{0.2}$)(C)N powder sample pyrolyzed at 1000 °C in NH_3 atmosphere; a) TEM-BF image of the particle bulk; inset in a) is the corresponding SAED pattern; b) HR-TEM image of the amorphous bulk region with the inset of the EDS spectrum of this area. c, d) HR-TEM images of the surface region showing TMCN precipitation; inset in c) shows the SAED pattern with distinct diffraction rings indexed as ($Ta_{0.8}Hf_{0.2}$)CN. The inset in d) represents the EDS spectrum of the crystalline TMCNs. Regions where the EDS spectra were taken are indicated by an asterisk in a) and d).

transition metals Hf and Ta and the K_α line of copper (originating from the commonly used copper grids) in EDS. The differentiation between Hf and Ta is more conclusive, when instead of copper grids, gold grids were used. For elemental analysis, the L-lines of Hf and Ta were chosen instead of the M-lines, because of the peak overlap of the Si-K peak and the Hf-/Ta-M peaks. With respect to the observed precipitates formed upon pyrolysis/annealing the EDS data are rather close to the overall composition of the precursors. For the Hf-rich system, a variation of Hf:Ta ranging between 0.63:0.37 and 0.77:0.23 was measured, while for the Ta-rich system a Ta:Hf ratio ranging from 0.85:0.15–0.78:0.22 was detected. Therefore, in the following, the compositions of the respective nanosized crystallites are given in the molar ratios of the precursors: $Hf_{0.7}Ta_{0.3}$ and $Ta_{0.8}Hf_{0.2}$, respectively.

It should be noted that, due to the pulverization of the powders for TEM analysis, the original microstructure of each powder particle was destroyed. Therefore, an additional preparation technique for SEM was necessary to verify the presence of different microstructural regions within the individual powder particles. After the initial pyrolysis and additional annealing steps, powder particles were embedded in an epoxy resin (SpeciFix-40, Struers, Copenhagen, Denmark). The usage of this cold epoxy resin prevented possible variation in microstructure caused by local heating. The preparation of the embedded powder particles then followed a standard ceramographic preparation technique with cutting, grinding, and polishing.

3. Results and discussion

Microstructural results of either Ta-rich (Si($Ta_{0.8}Hf_{0.2}$)(C)N) or Hf-rich (Si($Hf_{0.7}Ta_{0.3}$)(C)N) polymer-derived ceramics were found to show in general very similar microstructural characteristics. Therefore, in the following, electron microscopy results are presented exemplarily for either the Hf-rich or the Ta-rich samples, since only the molar ratios of Hf versus Ta had been altered during the polymer synthesis. The presented results on the powder samples represent the material characterization in general, however, please note that there is no potential application for the powders per se, instead these materials are intended

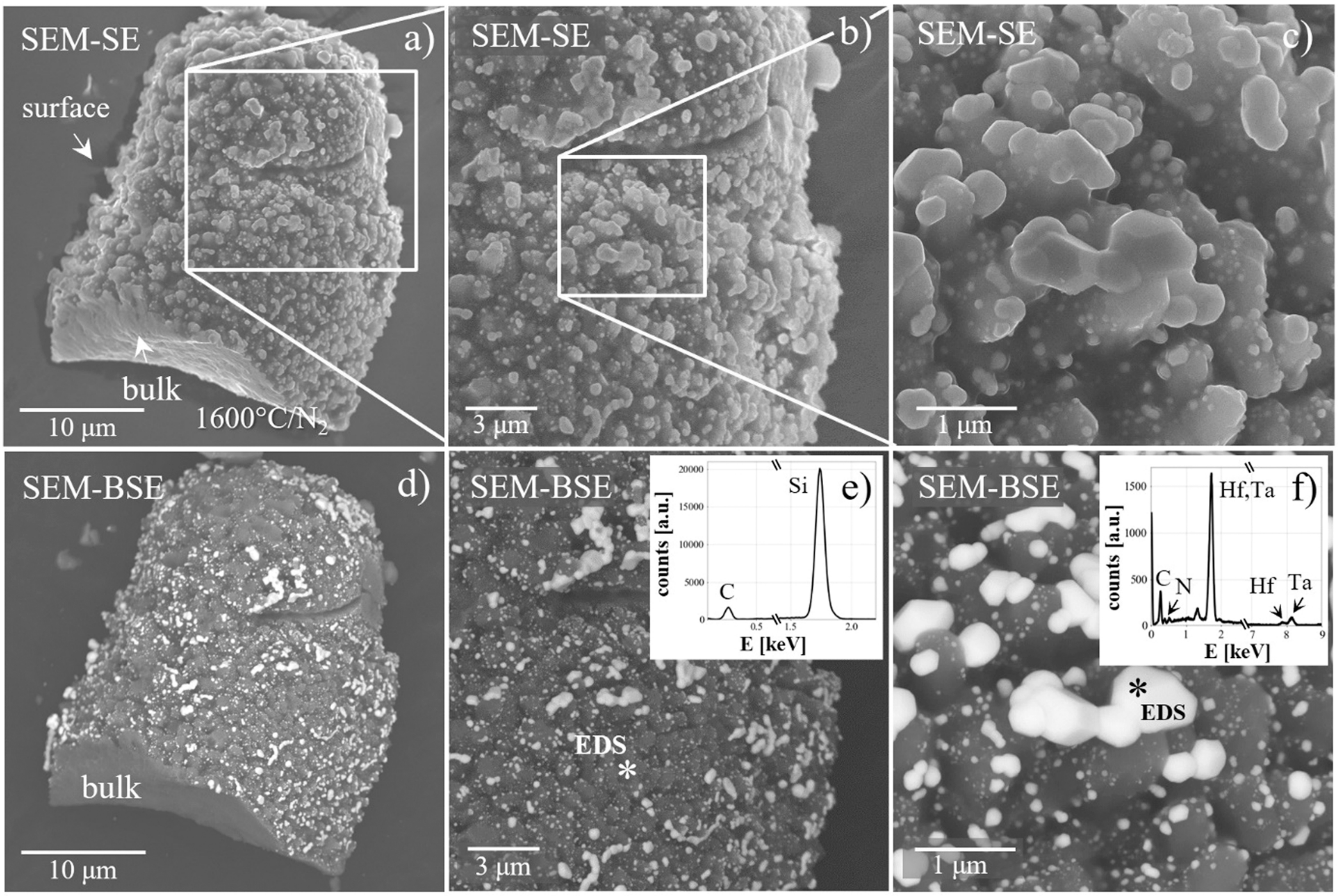

Fig. 6. SEM-SE (a-c) and SEM-BSE (d-f) images showing the microstructure of an individual powder particle of the $Si(Ta_{0.8}Hf_{0.2})(C)N$ sample upon 1600 °C annealing. Surface and bulk regions are displayed. Insets in (e) and (f) are EDS spectra originating from SiC and $(Ta_{0.8}Hf_{0.2})C$, respectively. The positions of the EDS measurements are indicated by an asterisk in e) and f).

serve as protective coatings for high-temperature alloys.

3.1. *X-ray powder diffraction (XRD) analysis*

The X-ray powder diffractograms of the $Si(Hf_xTa_{1-x})(C)N$ ceramics pyrolyzed at 1000 °C for 3 h are depicted in Fig. 3a. The patterns exhibit a pseudo-amorphous structure. The shape of the diffraction peaks from the 1000 °C powder samples is notably very broad. The pseudo-amorphous structure shows two wide humps around 17° and 30°, which can be ascribed to (Hf,Ta)C(N) nanodomains in the ceramic material. XRD has a detection limit of ~1–2 vol%; therefore, identification of low-content and nanosized precipitates, which formed at an early stage of pyrolysis, is rather difficult with XRD [21]. However, high-resolution SEM and TEM imaging clearly revealed the presence of such nanocrystals at the surface of the powder particles (compare also Fig. 4 and Fig. 5). Fig. 3b presents the X-ray powder diffractogram of the sample after annealing at 1600 °C in N_2. The pseudo-amorphous pattern has disappeared and sharp intensity reflections have developed. Annealing induces the crystallization of α-Si_3N_4 (PDF 41–0360), β-Si_3N_4(PDF 33–1160), β-SiC (PDF. 29–1129) and the solid solutions of the two transition metal carbides $(Ta_{0.8}Hf_{0.2})C$ and $(Hf_{0.7}Ta_{0.3})C$, as shown in the XRD patterns of the 1600 °C powder samples given in Fig. 3b. The underlying reflections for $(Hf_{0.7}Ta_{0.3})C$ refer to HfC (PDF 39–1491), whereas the reflections of $(Ta_{0.8}Hf_{0.2})C$ refer to TaC (PDF 35–0801).

Note that the unexpected formation of Ta/Hf carbides instead of nitrides at higher temperatures will be rationalized later in Section 3.3; compare also Fig. 9b and corresponding text.

3.2. *Microstructural analysis of as-pyrolyzed $Si(Hf_xTa_{1-x})(C)N$ at 1000 °C in NH_3*

The SEM micrographs in Fig. 4 show the microstructure of the $Si(Hf_{0.7}Ta_{0.3})(C)N$ ceramics pyrolyzed for 3 h at 1000 °C in NH_3 atmosphere for two different resolutions. Finely dispersed precipitates were observed on the surface of individual powder particles by high resolution-SEM (Fig. 4b,d). Secondary electron (SE) (Fig. 4b) and backscattered electron (BSE) images (Fig. 4d) clearly reveal the presence of nanoparticles on the surface of the ceramic particles. Grain sizes of these precipitates range from 5 to 50 nm and their morphology is nearly spherical (Fig. 4b). While the SEM-SE image in Fig. 4b provides information on the surface topography and the size of the nanoparticles, the SEM-BSE image in Fig. 4d highlights the chemical difference between the nanoparticles (white) and the underlying matrix phase (gray) due to its sensitivity to the atomic number (Z-contrast). The chemical analysis of the nanoparticles via EDS indicates an enrichment of Hf, (Ta), C and N (depicted by the continuous blue line in Fig. 4c). It should be noted that EDS measurements in SEM on nanosized crystallites suffer from the large interaction volume of the incident electron beam with the sample; therefore, resulting in deviations from the exact composition. Background and/or underlying phases are also recorded within single EDS-point measurements. Thus, it is assumed that the rather strong N peak (Fig. 4c) emerges from the underlying matrix phase, which primarily comprises Si, N and C (dashed red line).

The observations regarding small crystallites (nanoparticles) on the surfaces were confirmed during TEM analysis. TEM bright-field (TEM-BF) images reveal an interesting microstructure, containing two

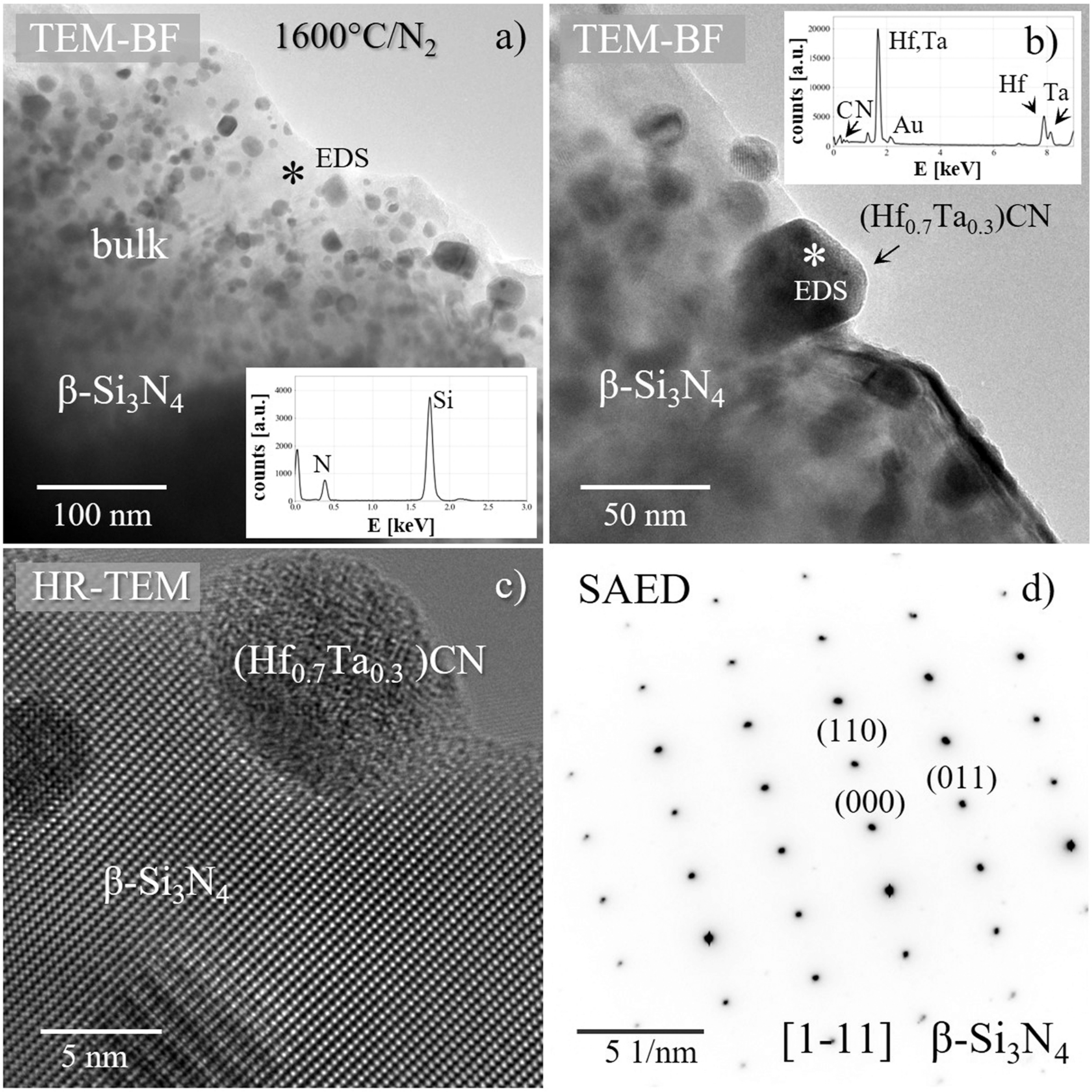

Fig. 7. TEM micrographs of a bulk region of the Si(Hf$_{0.7}$Ta$_{0.3}$)(C)N sample annealed at 1600 °C, showing the phase assemblage of beta-silicon nitride (β-Si$_3$N$_4$) and nanosized (Hf$_{0.7}$Ta$_{0.3}$)CN crystallites. TEM-BF images (a,b) with insets of EDS spectra of Si$_3$N$_4$ and (Hf$_{0.7}$Ta$_{0.3}$)CN. The exact location of each EDS measurement is indicated with an asterisk in a) and b). The SAED pattern in d) is obtained from β-Si$_3$N$_4$ oriented along [1–11] and corresponds to the HR-TEM image of β-Si$_3$N$_4$ shown in c).

distinctly different regions upon pyrolysis (Fig. 5). In the following, these two observed regions are considered as bulk and surface region of one initial powder particle. As already mentioned, the analyzed samples are powder samples. Therefore, every individual powder particle within the powder sample is defined as an individual system in this study. When studied by TEM, bulk regions reveal a featureless microstructure with a homogeneous amplitude contrast (Fig. 5a). The SAED pattern (inset in Fig. 5a), which exhibits a diffuse ring pattern in combination with the high-resolution TEM (HR-TEM) image (Fig. 5b), both indicate that these bulk regions are in fact amorphous. In contrast, the microstructure of the surface regions of the initial powder particle appears completely different. As already shown in the SEM micrographs in Fig. 4, the surface region shows small crystallites. The HR-TEM micrographs in Fig. 5c, d reveal nanosized crystallites ranging from 5 to 20 nm in the surface region, indicated by arrows. This size of the nanoparticles is slightly smaller than that observed by SEM, which is due to the specific region studied in TEM. Another reason for the small difference in the observed particle sizes could also be the different magnifications which are available in SEM vs. TEM. The SAED pattern originating from this region reveals distinct diffraction rings (inset in Fig. 5c), which is characteristic for the dispersion of crystalline nanosized particles. The ring-pattern could be indexed as a (Ta$_{0.8}$Hf$_{0.2}$)CN phase, indicating the formation of transition metal carbonitrides (TMCNs).

The observed regions differ in their microstructure and local chemistry. The insets in Fig. 5b,d indicate two EDS spectra giving the chemical compositions of the residual amorphous phase at the surface next to the TMCN precipitates shown here. The EDS spectrum of the amorphous area in Fig. 5b mainly shows intensities of Si, Hf, Ta, N, C and O. The EDS spectrum of the TMCN precipitates at surface regions (Fig. 5d) only contains Hf, Ta, C and N with a minor trace of O. Based on the chemical analysis in conjunction with electron diffraction, the precipitation of nanosized TMCNs at the surface of individual powder particles is proven.

TMCN-grain sizes at the surface and close to surface-near regions show a wide particle-size distribution, ranging from approximately 5 nm (Fig. 5d) to about 50 nm for the largest crystal size observed via SEM

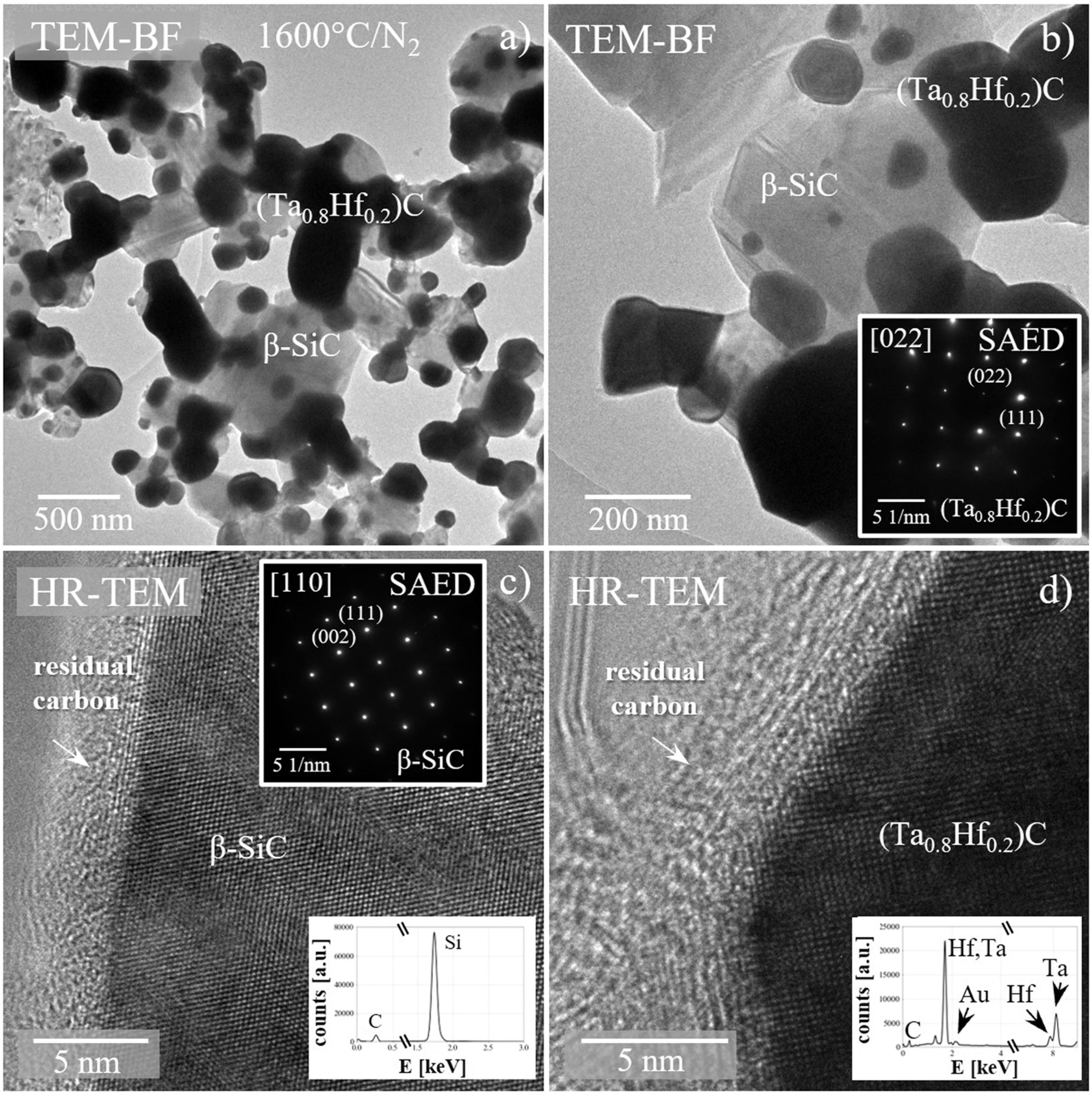

Fig. 8. TEM images (TEM-BF, HR-TEM, SAED pattern and EDS spectra) of the surface region of Si($Ta_{0.8}Hf_{0.2}$)(C)N annealed at 1600 °C, showing coarse ($Ta_{0.8}Hf_{0.2}$)C crystallites next to β-SiC. The dark and bright phases in (a) and (b) are TMCs and β-SiC, respectively; c) and d) reveal HR-TEM images of β-SiC and ($Ta_{0.8}Hf_{0.2}$)C both encapsulated by residual carbon; insets in (b), (c), and (d) show the corresponding SAED patterns and EDS spectra.

(Fig. 4b). The samples pyrolyzed at 1000 °C showed the presence of a 1–2 nm thin layer of segregated carbon around the transition metal carbonitrides (Fig. 5d). Such residual carbon existing as a carbon layer has been reported for similar PDC-related materials in the literature [30,32,42,43]. Regarding the amorphous bulk regions, also a small amount of carbon was detected by EDS as shown in the inset in Fig. 5b, indicating that the carbon phase is still incorporated within the glass network structure and has not yet undergone phase separation. From these results it can be inferred that the Si(Hf_xTa_{1-x})(C)N ceramic pyrolyzed at 1000 °C is composed of an amorphous Si-Hf-Ta-C-N-(O) host matrix with finely dispersed (Hf_xTa_{1-x})CN crystallites, mainly located at the surface of the powder particles. Note that in the amorphous bulk region a small amount of oxygen being incorporated during polymer processing; a well-known problem during PDC synthesis. Yuan et al. [27] reported on phase separation processes in Si-Hf-B-C-N-based ceramics starting at temperatures as low as 800 °C, similar results have been published for the Si-Hf-C-O system [27,44].

In comparison, the two systems studied, developed a very similar micro/nanostructure upon pyrolysis at 1000 °C, with an amorphous bulk and the precipitation of transition-metal carbonitrides at the surface-near region. There is no obvious difference between the two material systems.

3.3. Microstructural analysis of annealed Si(Hf_xTa_{1-x})(C)N at 1600 °C in N_2

The Si(Hf_xTa_{1-x})(C)N samples prepared upon pyrolysis at 1000 °C and annealed at 1600 °C for 3 h in N_2 atmosphere were studied by SEM and TEM to assess the microstructure evolution. Annealing at 1600 °C leads to a fully crystalline ceramic material with well-established surface and bulk regions of the individual powder particles. These two microstructurally different regions have already been observed in the pyrolyzed sample, however in a much less pronounced state (Fig. 4 and Fig. 5). After annealing, bulk and surface regions (ranging between 200 and 500 nm in thickness) exhibit differences in their phase assemblage and local chemistry, which is in particular noticeable in the grain-size distribution of the transition metal carbides (TMCs), which exclusively formed at high-temperature (Fig. 6). The SEM-SE and SEM-BSE

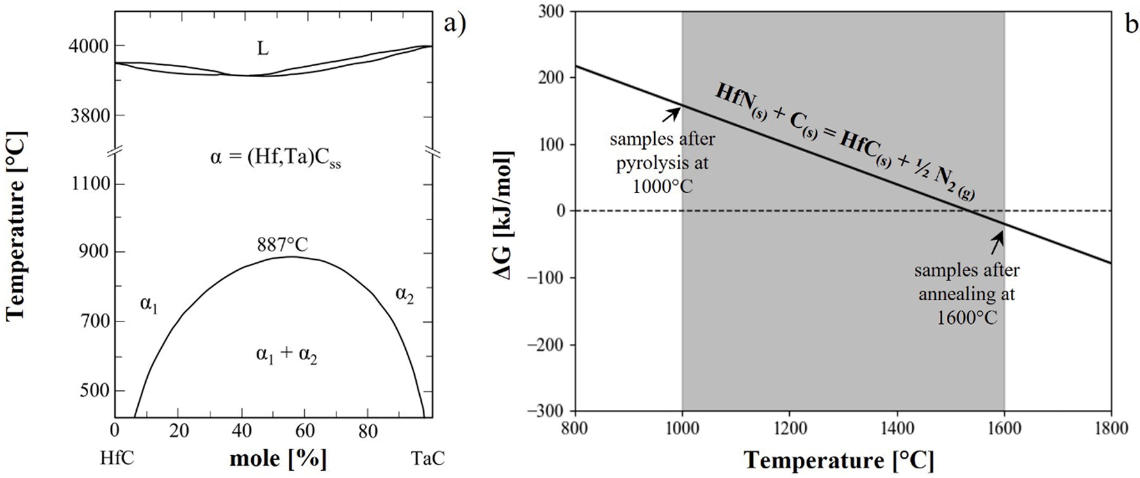

Fig. 9. a) Binary phase diagram of HfC and TaC showing a complete solid solution at high temperature and a miscibility gap below 887 °C (redrawn after Gusev et al. [46]). b) Ellingham diagram showing the temperature dependence of the change in the Gibbs free energy of the possible reaction of hafnium nitride plus free carbon decomposing into hafnium carbide plus gaseous nitrogen, occurring during HT annealing. The gray shaded area indicates the temperature range from pyrolysis at 1000 °C to high-temperature anneal at 1600 °C.
Diagram redrawn from Yuan et al. [27], data taken from Blum et al. [47].

micrographs in Fig. 6a-c and d-f, respectively, show the microstructure of an individual powder particle, mainly focusing on the surface region. The surface is characterized by a rough topography with rather coarse $(Ta_{0.8}Hf_{0.2})C$ grains. The bulk region (lower side part of the particle, see "bulk" in a and d) is composed of a dense and more homogeneous matrix phase, as indicated in Fig. 6a,d. Apart from the TMC crystallites, the previously amorphous surface regions are now crystallized to larger SiC grains (compare also Fig. 8b,c).

The TEM-BF images in Fig. 7a,b depict a typical microstructure appearing in the bulk regions. At this high temperature, the initially amorphous bulk underwent crystallization and phase separation resulting in Si_3N_4 with small TMCN crystallites. Fig. 7a,b contain an inset of an EDS spectrum each. The EDS spectrum in Fig. 7a shows Si and N; the spectrum in Fig. 7b contains Hf, Ta, C and N. The HR-TEM image in Fig. 7c represents the phase assemblage in the bulk region, with beta-silicon nitride (β-Si_3N_4) and the embedded nanosized TMCNs. The SAED pattern in Fig. 7d shows silicon nitride oriented along the [1–11] zone axis. The Si_3N_4 grains compose the matrix phase and can be as large as 1 µm in size, incorporating the nanosized $(Hf_{0.7}Ta_{0.3})CN$ particles which were first to crystallize. Therefore, via this crystallization process, the TMCNs are enclosed by the Si_3N_4.

TEM-BF, HR-TEM, SAED and EDS spectra given in Fig. 8 show a typical microstructure of a surface region. Within these surface regions, silicon carbide (β-SiC) and coarse $Hf_xTa_{1-x}C$ grains with grain sizes up to 200 nm are present. Transition metal carbides are depicted as dark grains in TEM-BF images (Fig. 8a,b). The HR-TEM images shown in Fig. 8c and Fig. 8d reveal that precipitates in surface-near regions are encapsulated by a thin carbon layer. The HR-TEM micrographs in conjunction with corresponding SAED patterns were employed to identify the crystalline phases β-SiC and $(Ta_{0.8}Hf_{0.2})C$. As reported in literature, cubic HfC and TaC with rock-salt (NaCl) structure form solid solutions (i.e., $Hf_xTa_{1-x}C$) [9]. The relationship between the lattice parameters and the x-values obey Vergard's law [2,9]. The standard lattice parameter of the stoichiometric HfC and TaC are 4.641 Å and 4.456 Å, respectively [45]. In addition to detecting TMCs, pure TaC was also confirmed, however rarely, within the phase assemblage of the Ta-rich powder sample as shown in Fig. 10d.

Annealing at 1600 °C induced pronounced crystallization in both bulk and surface-near region. Compared to the systems obtained at 1000 °C, the surface particle size strongly increased and additional gas-phase reactions, producing Si_3N_4 and SiC whiskers, altered the micro/nanostructure. Depending on the system analyzed, the Ta-rich sample revealed slightly larger TMC particles which were also highly faceted, giving sharper XRD patterns (compare Fig. 3). Moreover, in the Ta-rich sample, precipitation of pure TaC was observed very rarely, as shown in Fig. 10.

In the following we present a discussion on the evolution on the phase composition observed via SEM and TEM inspection, based on the literature. In the binary phase diagram reported by Gusev et al. [46], HfC and TaC form a continuous series of solid solution at temperatures exceeding 887 °C. As depicted in the phase diagram, there is a miscibility gap at lower temperatures, which rationalizes the presence of pure TaC (Fig. 9a) in the Ta-rich sample.

During TEM analysis, TM carbides instead of TM nitrides were found upon high-temperature anneal at 1600 °C. A possible explanation is the carbon availability within the system, because of remains of CH_3 groups even after the pyrolysis, originating from the polymeric precursors TDMAH and PDMAT. Initially, it was expected that the majority of the organic methyl groups of the dimethylamido complex $N(Me_2)_x$ with Me $= CH_3$, were released during the transamination reactions between NH_3 and NMe_2 (see also Fig. 1). Remaining methyl groups serve as the carbon source necessary for carbide or carbonitride formation. Yuan et al. [27] reported an explanation why carbides were found instead of nitrides using thermodynamics and the corresponding Ellingham diagram. As depicted in Fig. 9b, hafnium nitride phases plus segregated carbon decompose into hafnium carbide plus gaseous nitrogen at temperatures beyond 1500 °C [27,47] (Eq. 1).

$$HfN(s) + C(s) \rightarrow HfC(s) + 1/2N_2(g) \qquad (1)$$

XRD data in combination with TEM analysis undoubtedly prove the presence of TM carbides instead of nitrides at 1600 °C. Although the Ellingham diagram suggests that TM nitrides should be thermodynamically stable at 1000 °C, Ta-, Hf-carbonitrides were observed in both samples. Even though the pyrolysis in ammonia atmosphere would favor TM nitride formation the higher carbon content in the amorphous bulk is responsible for the observed TMCN crystallization at low temperature.

Both samples (Hf-rich and Ta-rich) annealed at 1600 °C in N_2 atmosphere showed amorphous free carbon at the surface regions (Fig. 10). HR-TEM micrographs revealed a thin carbon layer, encapsulating the TMC particles (Fig. 10b,d). This so-called carbon shell was found as a 2–5 nm thin rim around every carbide particle (as also observed in studies reported by Wen et al. [30]). Due to this frequently made observation of carbon layers at the surface of TMCN and TMC particles, it is assumed that surface-diffusion is the cause for the

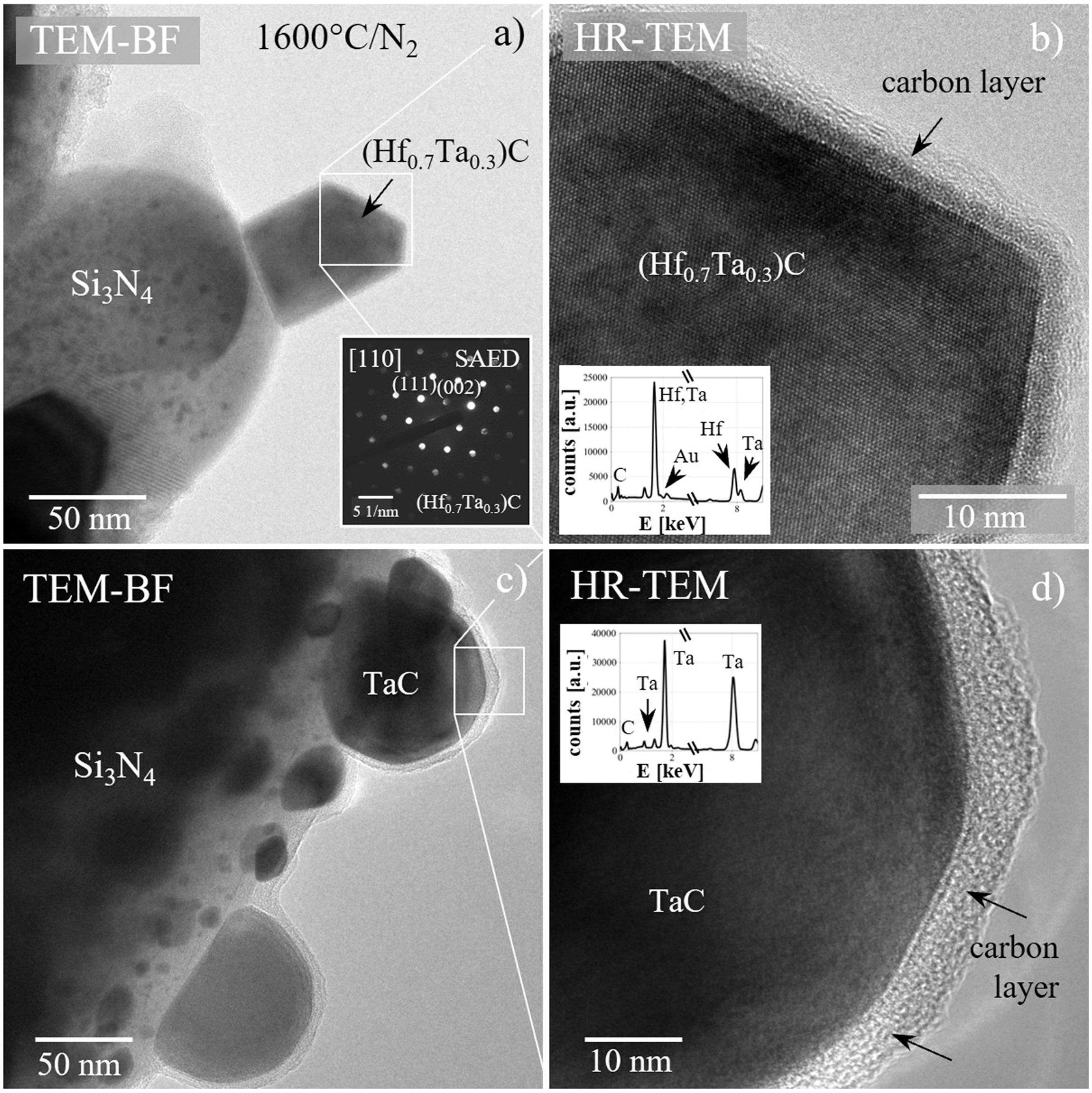

Fig. 10. TEM-BF micrographs of transition metal carbides observed in the Hf-rich $Si(Hf_{0.7}Ta_{0.3})(C)N$ (a,b) and Ta-rich $Si(Ta_{0.8}Hf_{0.2})(C)N$ (c,d) ceramic sample, annealed at 1600 °C in N_2 atmosphere; amorphous carbon surface layers are found in both samples, encapsulating the TMC particles. Note that besides $(Hf_xTa_{1-x})C$ also pure TaC precipitates, as depicted in d), were rarely detected.

formation of these thin carbon layers.

3.4. *Thermal decomposition reactions*

Solid solution precipitates (TMCs and TMCNs) vary in their grain size, depending on whether they are located in the bulk or in the surface region, investigated in the fractured and polished cross section of the powder aggregates (Fig. 7, Fig. 12). When $(Hf_xTa_{1-x})CN$ is found in the bulk region, the TMCNs show relatively small grains of up to 50 nm upon pyrolysis at 1000 °C, the embedding host matrix around them consists of Si-Hf-Ta-C-N-(O). High-temperature anneal at 1600 °C results solely in Hf-, Ta-carbide formation showing an increased particle size with a maximum diameter of approximately 500 nm, coexisting with β-SiC. The decomposition of Si_3N_4 is accompanied by the enhanced depletion of volatiles such as N_2 at the surface (compare EDS data in Fig. 12). This commonly known thermal decomposition reaction [48], where solid Si_3N_4 decomposes and reacts with carbon to form solid SiC and gaseous nitrogen, is given in Eq. 2.

$$Si_3N_4(s) + 3C(s) \rightarrow 3\beta SiC(s) + 2N_2(g) \quad (2)$$

The thermal decomposition reaction (Eq. 2) is well known in literature and tends to start at temperatures exceeding 1440 °C in N_2 atmosphere [48–51]. The thermal decomposition of Si_3N_4 in the annealed ceramics leads to an increased volume fraction of SiC in the surface region. It is assumed that the diffusion of the transition metals in surface regions (SiC-rich) is faster along amorphous carbon layers than the diffusion in the Si_3N_4-rich bulk. Consequently, since Si_3N_4 is still present in the bulk, it contains small TMCN precipitates, whereas in surface-near regions larger TM-carbides and large β-SiC grains are found. This decomposition reaction is undoubtedly one main reason for the observed different microstructural evolution of surface and bulk upon high-temperature anneal, which in fact is already initiated at pyrolysis temperature.

3.5. *Vapor-phase reactions*

Individual powder particles show surface regions with abnormal grain growth of Si_3N_4 and SiC. Columnar Si_3N_4 and whisker-like SiC crystallites with high aspect ratios were observed at the powder particle

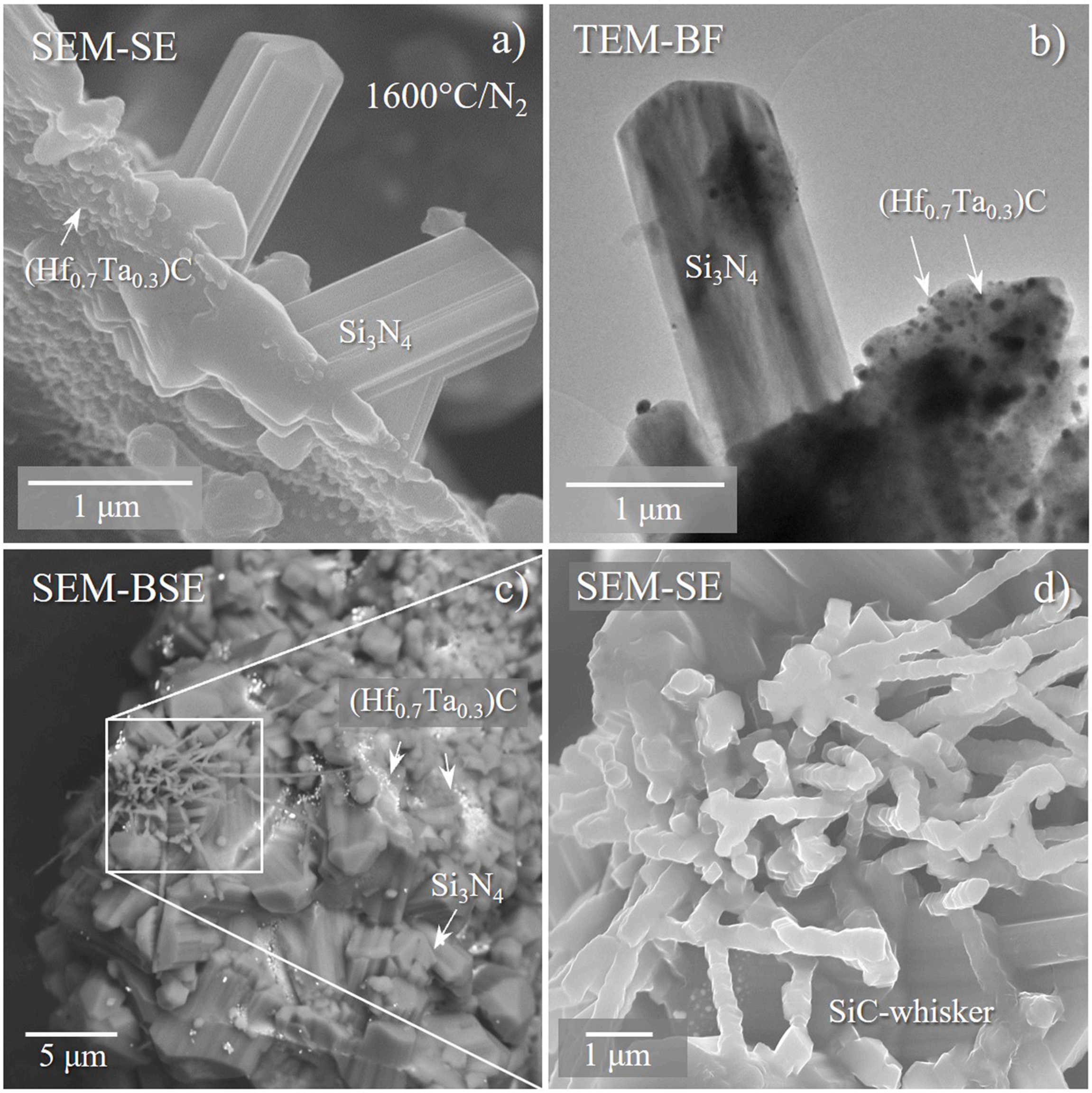

Fig. 11. SEM-SE (a,d), SEM-BSE (c) and TEM-BF (b) micrographs of pronounced crystal growth at the particle surface of Si(Hf$_{0.7}$Ta$_{0.3}$)(C)N annealed at 1600 °C as a result of local vapor-phase reactions. Idiomorphic silicon nitride (Si$_3$N$_4$) crystals next to silicon carbide (SiC) whiskers are observed.

surface both in SEM and TEM analysis. They are assumed to emerge from local vapor-phase reactions during the high-temperature anneal (Fig. 11).

The nitrogen atmosphere and the release of nitrogen at elevated temperature (decomposition of Si$_3$N$_4$) supports vapor-phase reactions, in particular, at the particle surface. This leads to a pronounced decoration of the outer particle surface with large idiomorphic Si$_3$N$_4$ grains and SiC whiskers (Fig. 11). Similar observations have been reported on SiCN- and SiCO-based PDCs [52–54].

3.6. Bulk/surface transition zone - diffusion phenomena and the influence of oxygen

Due to the preparation technique involving grinding of the powder particles for the TEM analysis to achieve electron transparency, the original microstructure was destroyed in its integrity. In consequence, bulk and surface regions were hardly ever observed together within one fragment of the powder particle in the TEM. Thus, the transition zone between bulk and surface could not be imaged. Therefore, additional SEM analysis was performed on a cross-section of polished individual powder particles, to confirm the presence of a microstructural gradient between bulk and surface. Fig. 12 shows two SEM-BSE images, giving an overview of the macrostructure of a single powder particle of the annealed Si(Hf$_{0.7}$Ta$_{0.3}$)(C)N sample. TM particles are visible as white dots in the BSE images, especially near the particle surface. In Fig. 12a, a distinct increase in particle size of TM precipitates from the inner bulk towards the outer surface region can be identified. The TMCN particles within the bulk region are up to 50 nm in size, whereas in contrast, TMCs in surface-near regions can be as large as 500 nm in diameter (Fig. 12b).

These variations in particle size seem to be a consequence of local chemical changes within the bulk and the surface-near region in each powder particle. To verify this, a distinct region of grain coarsening from bulk to surface was analyzed by EDS. Fig. 12b shows the SEM-BSE image of the transition zone and the selected region for EDS analysis. EDS point measurements were taken only in the gray matrix phase (not in the white TMCs) to gain information on the chemical changes in the transition zone between bulk and surface, however, excluding the TMC precipitates as much as possible. The corresponding graph in Fig. 12c depicts the change in the relative concentration of Si, C, N, O, Hf, and Ta,

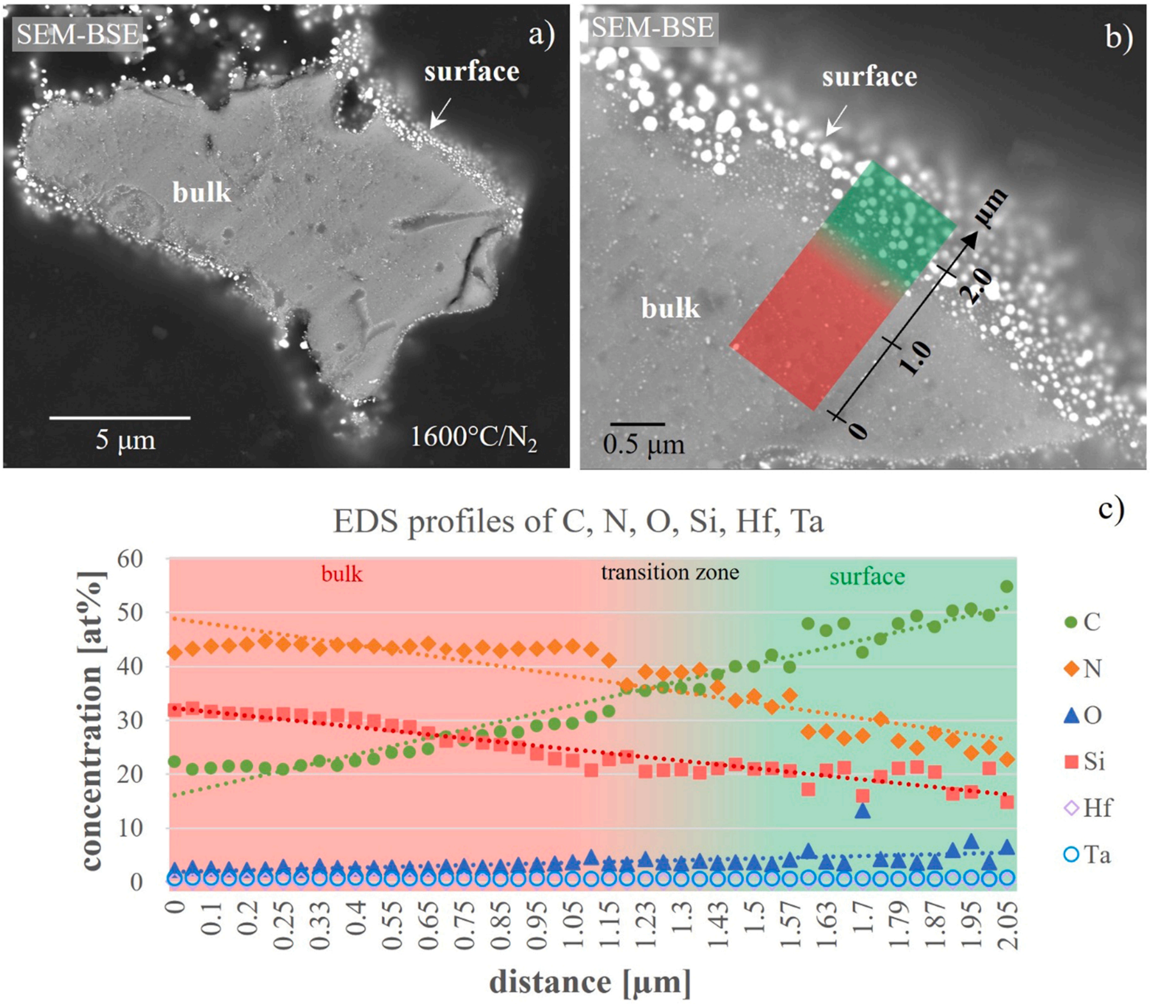

Fig. 12. a, b) SEM-BSE micrographs of a cross-section of an individual powder particle ($Si(Hf_{0.7}Ta_{0.3})(C)N$) annealed at 1600 °C with grain coarsening from inner bulk to outer surface regions; c) relative concentrations of C, N, O, Si, Hf and Ta in the matrix phase as measured by EDS. The concentrations of Si, C, N and O are clearly related to the grain coarsening and therefore depend on the distance to the surface. The $(Hf_{0.7}Ta_{0.3})C$ particle size distribution follows the C, N and O concentration profiles in a systematic manner: the particle size of the solid solutions increases in the surface-near region, where in particular the O content is increased, favouring both diffusion processes and grain growth.

when moving from the bulk to the surface region (from left to right).

Two concentration profiles of C and N (circle and diamond symbol) show an inverse curve characteristic. The carbon content increases from bulk to surface, whereas the nitrogen shows the exact opposite behavior. These two profiles intersect at ~1.2 1.4 µm from the starting point of the EDS measurement. Compared to the SEM-BSE image in Fig. 12b, this matches exactly the transition zone between bulk and surface. This supports the observations made via TEM, where nitrogen is predominantly present in the bulk region forming mainly silicon nitride. Carbon tends to concentrate in the surface regions, forming β-SiC and residual carbon layers. This observation can be explained with the thermal decomposition reaction of Si_3N_4, as described earlier in Section 3.4. Additionally, the oxygen concentration (triangle symbol) shows an increase from roughly 2 at% up to 8 at%, which is rather high for carbonitridic PDCs.

This finding of coarsening in combination with local changes in chemistry are comparable to experimental results reported in literature [39,40,55–57]. Kleebe et al. [40] described a similar coarsening behavior of HfO_2 particles embedded within a polymer-derived SiHfCO matrix upon isothermal heat treatment at 1300 °C. The authors showed that a pronounced grain coarsening of hafnia at surface-near regions occurs due to a decreased carbon content in the area, leading to a higher diffusion coefficient of Hf in the silica matrix [40], resulting in an enhanced particle growth. They proposed a decomposition-coarsening model, explaining the observed particle size variations in Si-Hf-C-O polymer-derived ceramics. Anand et al. [55] described a diffusion-controlled coarsening of ZrO_2 crystallites in a Si-C-N-O ceramic. Significant coarsening of nanoparticles was also reported by Sujith et al. [57], who showed that the coarsening of nanosized hafnia in Si-Hf-C-N-O can be explained by diffusion-controlled processes and local chemical variations.

For the samples studied here, the oxygen content seems to modify the diffusivity of Hf and Ta in such a way that a distinct coarsening of TMCs in the surface-near regions is feasible. As shown in Fig. 12c, the oxygen concentration increases close to the particle surface. It is assumed that the oxygen content originates from the polymer synthesis process, representing an unwanted but common impurity. A faster elemental diffusion of Hf and Ta caused by an increased oxygen concentration, in conjunction with a decrease in nitrogen (decomposition of Si_3N_4) and the presence of amorphous carbon in surface-near regions, seems to lead to the observed TMC coarsening.

3.7. *Microstructural evolution from 1000 °C to 1600 °C*

The microstructural evolution of the $Si(Hf_xTa_{1\ x})(C)N$ system upon thermal treatment is schematically sketched in Fig. 13. The image shows

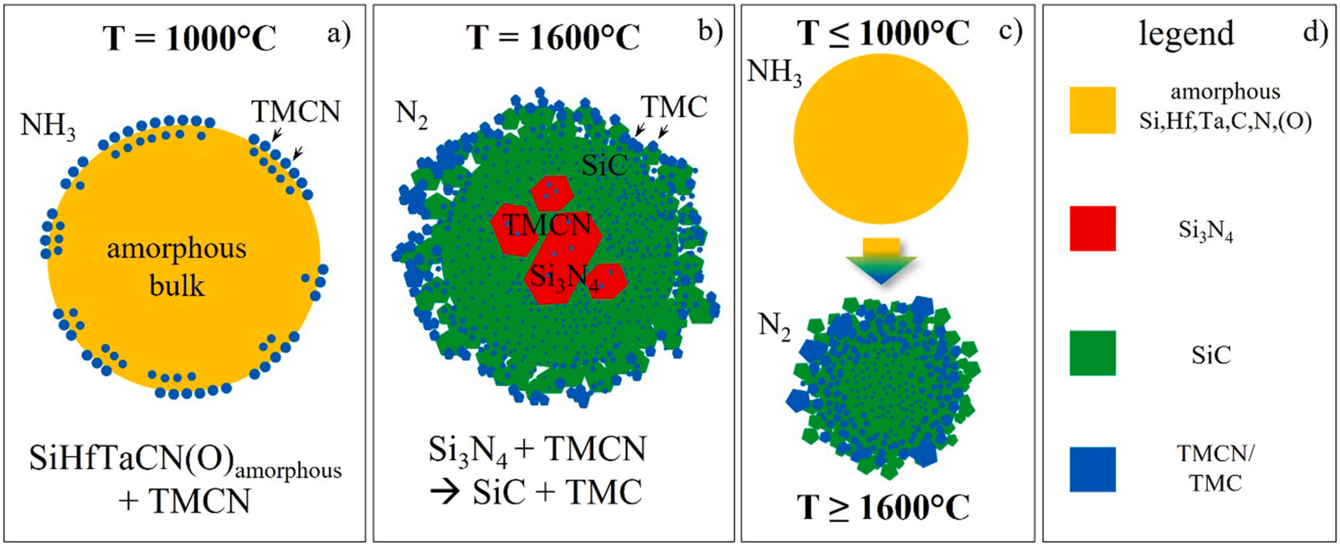

Fig. 13. Schematic illustrating the phase evolution of Si(Hf,Ta)(C)N ceramics upon pyrolysis and subsequent high-temperature anneal. In a) it is shown that the bulk is mostly amorphous with minor crystallization of TMCNs in the surface-near region. In b) the phase evolution upon annealing at 1600 °C is shown where the bulk is composed of Si_3N_4 with small TMCNs embedded, while the surface region is characterized by larger TMC particles and SiC crystallites. The schematics in c) represent the assumed phase evolution at temperatures below 1000 °C and above 1600 °C. Note that no crystallization is expected at low temperature, while at high temperature there is no longer Si_3N_4 present. In d) the legend of the phases observed is given.

four individual powder particles, starting with the initially amorphous particle at $T < 1000$ °C and its stepwise crystallization upon heat treatment. The final microstructure of the particle relates to an annealing temperature of $T > 1600$ °C.

Beginning with a featureless amorphous microstructure, the evolution in the $Si(Hf_xTa_{1-x})(C)N$ polymer-derived powder samples proceeds as follows upon heat treatment at 1600 °C in N_2 atmosphere: based on the XRD data, the as-prepared sample is X-ray amorphous and consists of a single Si-Hf-Ta-C-N-(O) phase (Fig. 13a). SEM and TEM analysis reveal that the powder particles show an amorphous and featureless microstructure in the bulk regions. In contrast, the surface regions reveal early crystallization of TMCN particles at 1000 °C (Fig. 13a).

At 1600 °C, bulk and surface regions undergo a continuous crystallization process. The evolution of surface and bulk regions within the powder samples annealed at 1600 °C is further advanced as compared to the samples pyrolyzed at 1000 °C (Fig. 13b). The early crystallization state of the surface regions at 1000 °C now converts into a matrix consisting of SiC with larger crystalline TMC particles (Fig. 13b). The surface regions undergo a carbothermal decomposition reaction, where Si_3N_4 decomposes into SiC and gaseous nitrogen (Eq.1) (Fig. 13b). In contrast to the surface area, the bulk region is composed of large crystalline Si_3N_4 grains with TMCNs embedded in them. In the interior of the powder particles, the decomposition of Si_3N_4 has not yet started. Hence, this crystallization/decomposition process is driven from the outside to the inside. In addition, the formation of $(Hf_xTa_{1-x})C$ or $(Ta_xHf_{1-x})C$ with their increased particle size at the surface is due to diffusion-controlled coarsening phenomena (Fig. 13b). At temperatures exceeding 1600 °C, a progression of the Si_3N_4 decomposition and further coarsening occurs, resulting in the thermodynamically stable phases of SiC and $(Hf_xTa_{1-x})C$ (Fig. 13c).

4. Conclusions

Ultra-high temperature ceramic (UHTC) powder samples of $Si(Hf_xTa_{1-x})(C)N$ composition were prepared by a single-source-precursor synthesis route. The microstructural evolution with respect to phase composition and crystallization behavior of this material class was characterized by XRD, SEM and TEM imaging including EDS analysis. Upon pyrolysis at 1000 °C, the obtained powder samples show early crystallization of transition metal carbonitrides (TMCNs), taking place in surface-near regions, while the bulk regions stayed predominantly amorphous. The unexpected formation of TM carbonitrides instead of nitrides could be rationalized by a higher amount of carbon (remaining CH_3-groups) in the precursor which can react with for example (Hf,Ta)N forming (Hf,Ta)CN. The most important finding is the different microstructural evolution of surface versus bulk. This characteristic microstructure feature is even more pronounced upon annealing at elevated temperatures, i.e., annealing at 1600 °C. At this temperature, a thermal decomposition reaction is induced in which the matrix phase, consisting of Si_3N_4, decomposes into SiC and gaseous nitrogen. The TMCs show a pronounced grain coarsening in surface-near regions. While Si_3N_4 is still present in the bulk, SiC was exclusively observed in surface regions. Local changes in chemistry; i.e., different amounts of C, N and/or O in the amorphous bulk are suggested to affect the diffusion of the transition metals. This should lead to the increased TMC grain size, in particular, in the surface-near region with its higher oxygen content and where the amorphous carbon layers were observed. Local decomposition in surface-near regions and the corresponding TMC particle coarsening is an active and characteristic mechanism in the $Si(Hf_xTa_{1-x})(C)N$-based polymer-derived ceramics upon annealing; a process which always has to be taken into account, when high-temperature applications of this material class are considered.

Declaration of Competing Interest

The authors declare that they have no known competing financial interests or personal relationships that could have appeared to influence the work reported in this paper.

Acknowledgement

The authors gratefully acknowledge the financial support provided by the Research Training Group 2561 “MatCom-ComMat: Materials Compounds from Composite Materials for Applications in Extreme Conditions” (project number: 413956820), funded by the Deutsche Forschungsgemeinschaft (DFG), Bonn, Germany.

References

[1] W.G. Fahrenholtz, G.E. Hilmas, Ultra-high temperature ceramics: materials for extreme environments, Scr. Mater. 129 (2017) 94–99, https://doi.org/10.1016/j.scriptamat.2016.10.018.

[2] S. Urbonaite, M. Johnsson, G. Svensson, Synthesis of $TiC_{1-x}N_x$ and $TaC_{1-x}N_x$ by spark plasma sintering, J. Mater. Sci. 39 (2004) 1907–1911, https://doi.org/10.1023/B:JMSC.0000016216.61410.4e.

[3] Q. Wen, R. Riedel, E. Ionescu, Solid-solution effects on the high-temperature oxidation behavior of polymer-derived (Hf,Ta)C/SiC and (Hf,Ti)C/SiC ceramic nanocomposites, Adv. Eng. Mater. 21 (2019) 1800879, https://doi.org/10.1002/adem.201800879.

[4] Z. Li, Y. Wang, X. Xiong, X. Li, Z. Chen, W. Sun, Microstructure and growth behavior of Hf(Ta)C ceramic coating synthesized by low pressure chemical vapor deposition, J. Alloy. Compd. 705 (2017) 79–88, https://doi.org/10.1016/j.jallcom.2017.02.101.

[5] G. Barroso, Q. Li, R.K. Bordia, G. Motz, Polymeric and ceramic silicon-based coatings – a review, J. Mater. Chem. A 7 (2019) 1936–1963, https://doi.org/10.1039/C8TA09054H.

[6] W.G. Fahrenholtz, G.E. Hilmas, I.G. Talmy, J.A. Zaykoski, Refractory diborides of zirconium and hafnium, J. Am. Ceram. Soc. 90 (2007) 1347–1364, https://doi.org/10.1111/j.1551-2916.2007.01583.x.

[7] E. Wuchina, E. Opila, M. Opeka, W.G. Fahrenholtz, I. Talmy, UHTCs: ultra-high temperature ceramic materials for extreme environment applications, Electrochem. Soc. Interface (2007) 30–36, https://doi.org/10.1149/2.F04074IF.

[8] E. Ionescu, S. Bernard, R. Lucas, P. Kroll, S. Ushakov, A. Navrotsky, R. Riedel, Polymer-derived ultra-high temperature ceramics (UHTCs) and related materials, Adv. Eng. Mater. 21 (2019) 1900269, https://doi.org/10.1002/adem.201900269.

[9] H.O. Pierson, Handbook of Refractory Carbides and Nitrides: Properties, Characteristics, Processing, and Applications, Noyes Publ, Westwood, NJ, 1996.

[10] E. Wuchina, M. Opeka, S. Causey, K. Buesking, J. Spain, A. Cull, J. Routbort, F. Guitierrez-Mora, Designing for ultrahigh-temperature applications: the mechanical and thermal properties of HfB_2, HfC_x, HfN_x and Hf(N), J. Mater. Sci. 39 (2004) 5939–5949, https://doi.org/10.1023/B:JMSC.0000041690.06117.34.

[11] S.A. Ghaffari, M.A. Faghihi-Sani, F. Golestani-Fard, M. Nojabayy, Diffusion and solid solution formation between the binary carbides of TaC, HfC and ZrC, Int. J. Refract. Met. Hard Mater. 41 (2013) 180–184, https://doi.org/10.1016/j.ijrmhm.2013.03.009.

[12] A. Bellosi, F. Monteverde, D. Sciti, Fast densification of ultra-high-temperature ceramics by spark plasma sintering, Int. J. Appl. Ceram. Technol. 3 (2006) 32–40, https://doi.org/10.1111/j.1744-7402.2006.02060.x.

[13] S.Z. Nazarova, E.Z. Kurmaev, N.I. Medvedeva, A. Mowes, Physical properties and electronic structure of TaC-HfC solid solutions, Russ. J. Inorg. Chem. 52 (2007) 233–237, https://doi.org/10.1134/S0036023607020155.

[14] O. Gaballa, B.A. Cook, A.M. Russell, Reduced-temperature processing and consolidation of ultra-refractory Ta_4HfC_5, IJRMHM 41 (2013) 293–299, https://doi.org/10.1016/j.ijrmhm.2013.04.018.

[15] Q. Wen, Z. Yu, R. Riedel, E. Ionescu, Significant improvement of high-temperature oxidation resistance of HfC/SiC ceramic nanocomposites upon incorporation of a small amount of boron, J. Eur. Ceram. Soc. 40 (2020) 3499–3508, https://doi.org/10.1016/j.jeurceramsoc.2020.03.067.

[16] L. Silvestroni, D. Sciti, J. Kling, S. Lauterbach, H.-J. Kleebe, Sintering mechanisms of zirconium and hafnium carbides doped with MoSi 2, J. Am. Ceram. Soc. 92 (2009) 1574–1579, https://doi.org/10.1111/j.1551-2916.2009.03049.x.

[17] D. Sciti, L. Silvestroni, S. Guicciardi, D.D. Fabbriche, A. Bellosi, Processing, mechanical properties and oxidation behavior of TaC and HfC composites containing 15 vol% $TaSi_2$ or $MoSi_2$, J. Mater. Res. 24 (2009) 2056–2065, https://doi.org/10.1557/jmr.2009.0232.

[18] F. Monteverde, A. Bellosi, Microstructure and properties of an HfB_2-SiC composite for ultra high temperature applications, Adv. Eng. Mater. 6 (2004) 331–336, https://doi.org/10.1002/adem.200400016.

[19] W.C. Tripp, H.H. Davis, H.C. Graham, Effect of an SiC addition on the oxidation of ZrB_2, Am. Ceram. Soc. Bull. 52 (1973) 612–616.

[20] E. Ionescu, G. Mera, R. Riedel, Polymer-derived ceramics (PDCs), in: I.M. Low, Y. Sakka, C.F. Hu (Eds.), MAX Phases and Ultra-High Temperature Ceramics for Extreme Environments, IGI Global, 2013, pp. 203–245.

[21] P. Colombo, G. Mera, R. Riedel, G.D. Sorarù, Polymer-derived ceramics: 40 years of research and innovation in advanced ceramics, in: J. Am. Ceram. Soc., 93, 2010, pp. 1805–1837, https://doi.org/10.1111/j.1551-2916.2010.03876.x (S.).

[22] R. Riedel, G. Mera, R. Hauser, A. Klonczynski, Silicon-based polymer-derived ceramics: synthesis properties and applications-a review, Nippon Seramikkusu Kyokai gakujutsu ronbunshi 114 (2006) 425–444, https://doi.org/10.2109/jcersj.114.425.

[23] B. Feng, J. Peter, C. Fasel, Q. Wen, Y. Zhang, H.-J. Kleebe, E. Ionescu, High-temperature phase and microstructure evolution of polymer-derived SiZrCN and SiZrBCN ceramic nanocomposites, J. Am. Ceram. Soc. 103 (2020) 7001–7013, https://doi.org/10.1111/jace.17149.

[24] Y.C. Song, Y. Zhao, C.X. Feng, Y. Lu, Synthesis and pyrolysis of polysilazane as the precursor of Si_3N_4/SiC ceramic, J. Mater. Sci. 29 (1994) 5745–5756, https://doi.org/10.1007/BF00349975.

[25] C. Zhou, X. Gao, Y. Xu, G. Buntkowsky, Y. Ikuhara, R. Riedel, E. Ionescu, Synthesis and high-temperature evolution of single-phase amorphous Si–Hf–N ceramics, J. Eur. Ceram. Soc. 35 (2015) 2007–2015, https://doi.org/10.1016/j.jeurceramsoc.2015.01.026.

[26] Q. Wen, Y. Xu, B. Xu, C. Fasel, O. Guillon, G. Buntkowsky, Z. Yu, R. Riedel, E. Ionescu, Single-source-precursor synthesis of dense SiC/HfC_XN_{1-x}-based ultrahigh-temperature ceramic nanocomposites, Nanoscale 6 (2014) 13678–13689, https://doi.org/10.1039/c4nr03376k.

[27] J. Yuan, S. Hapis, H. Breitzke, Y. Xu, C. Fasel, H.-J. Kleebe, G. Buntkowsky, R. Riedel, E. Ionescu, Single-source-precursor synthesis of hafnium-containing ultrahigh-temperature ceramic nanocomposites (UHTC-NCs), Inorg. Chem. 53 (2014) 10443–10455, https://doi.org/10.1021/ic501512p.

[28] J. Yuan, D. Li, K.E. Johanns, C. Fasel, K. Durst, H.-J. Kleebe, Z. Shen, R. Riedel, E. Ionescu, Preparation of dense SiHf(B)CN-based ceramic nanocomposites via rapid spark plasma sintering, J. Eur. Ceram. Soc. 37 (2017) 5157–5165, https://doi.org/10.1016/j.jeurceramsoc.2017.04.066.

[29] W. Yi, X. Yongdong, W. Yiguang, C. Laifei, Z. Litong, Effects of TaC addition on the ablation resistance of C/SiC, Mater. Lett. 64 (2010) 2068–2071, https://doi.org/10.1016/j.matlet.2010.04.051.

[30] Q. Wen, Z. Yu, Y. Xu, Y. Lu, C. Fasel, K. Morita, O. Guillon, G. Buntkowsky, E. Ionescu, R. Riedel, SiC/$Hf_yTa_{1-y}C_xN_{1-x}$/c ceramic nanocomposites with $Hf_yTa_{1-y}C_xN_{1-x}$-carbon core-shell nanostructure and the influence of the carbon-shell thickness on electrical properties, J. Mater. Chem. 6 (2018) 855–864, https://doi.org/10.1039/C7TC05023B.

[31] S.A. Ghaffari, M.A. Faghihi-Sani, F. Golestani-Fard, H. Mandal, Spark plasma sintering of TaC–HfC UHTC via disilicides sintering aids, J. Eur. Ceram. Soc. 33 (2013) 1479–1484, https://doi.org/10.1016/j.jeurceramsoc.2013.01.017.

[32] Q. Wen, Z. Yu, R. Riedel, E. Ionescu, Single-source-precursor synthesis and high-temperature evolution of a boron-containing SiC/HfC ceramic nano/micro composite, J. Eur. Ceram. Soc. 41 (2021) 3002–3012, https://doi.org/10.1016/j.jeurceramsoc.2020.05.031.

[33] T. Konegger, C.C. Tsai, R.K. Bordia, Preparation of polymer-derived ceramic coatings by dip-coating, 20th Symposium on Composites 825–826 (2015) 645–652, https://doi.org/10.4028/www.scientific.net/MSF.825-826.645.

[34] N.P. Padture, M. Gell, E.H. Jordan, Thermal barrier coatings for gas-turbine engine applications, Science 296 (2002) 280–284, https://doi.org/10.1126/science.1068609.

[35] B. Papendorf, K. Nonnenmacher, E. Ionescu, H.-J. Kleebe, R. Riedel, Strong influence of polymer architecture on the microstructural evolution of hafnium-alkoxide-modified silazanes upon ceramization, Small 7 (2011) 970–978, https://doi.org/10.1002/smll.201001938.

[36] E. Ionescu, B. Papendorf, H.-J. Kleebe, H. Breitzke, K. Nonnenmacher, G. Buntkowsky, R. Riedel, Phase separation of a hafnium alkoxide-modified polysilazane upon polymer-to-ceramic transformation-a case study, J. Eur. Ceram. Soc. 32 (2012) 1873–1881, https://doi.org/10.1016/j.jeurceramsoc.2011.09.003.

[37] E. Ionescu, B. Papendorf, H.-J. Kleebe, R. Riedel, Polymer-derived silicon oxycarbide/hafnia ceramic nanocomposites. Part II: stability toward decomposition and microstructure evolution at $T \gg 1000^\circ C$, J. Am. Ceram. Soc. 93 (2010) 1783–1789, https://doi.org/10.1111/j.1551-2916.2009.03527.x.

[38] B. Papendorf, E. Ionescu, H.-J. Kleebe, C. Linck, O. Guillon, K. Nonnenmacher, R. Riedel, High-temperature creep behavior of dense SiOC-based ceramic nanocomposites: microstructural and phase composition effects, J. Am. Ceram. Soc. 96 (2013) 272–280, https://doi.org/10.1111/jace.12067.

[39] K. Nonnenmacher, H.-J. Kleebe, J. Rohrer, E. Ionescu, R. Riedel, Carbon mobility in $SiOC/HfO_2$ ceramic nanocomposites, J. Am. Ceram. Soc. 96 (2013) 2058–2060, https://doi.org/10.1111/jace.12440.

[40] H.-J. Kleebe, K. Nonnenmacher, E. Ionescu, R. Riedel, Decomposition-coarsening model of $SiOC/HfO_2$ ceramic nanocomposites upon isothermal anneal at 1300°C, J. Am. Ceram. Soc. 95 (2012) 2290–2297, https://doi.org/10.1111/j.1551-2916.2012.05227.x.

[41] J. Yuan, M. Galetz, X.G. Luan, C. Fasel, R. Riedel, E. Ionescu, High-temperature oxidation behavior of polymer-derived SiHfBCN ceramic nanocomposites, J. Eur. Ceram. Soc. 36 (2016) 3021–3028, https://doi.org/10.1016/j.jeurceramsoc.2015.12.006.

[42] Q. Wen, Z. Yu, R. Riedel, The fate and role of in situ formed carbon in polymer-derived ceramics, Prog. Mater. Sci. 109 (2020), 100623, https://doi.org/10.1016/j.pmatsci.2019.100623.

[43] Y. Lu, Y. Sun, T. Zhang, F. Chen, L. Ye, T. Zhao, Polymer-derived Ta_4HfC_5 nanoscale ultrahigh-temperature ceramics: synthesis, microstructure and properties, J. Eur. Ceram. Soc. 39 (2019) 205–211, https://doi.org/10.1016/j.jeurceramsoc.2018.10.012.

[44] E. Ionescu, H.-J. Kleebe, R. Riedel, Silicon-containing polymer-derived ceramic nanocomposites (PDC-NCs): preparative approaches and properties, Chem. Soc. Rev. 41 (2012) 5032–5052, https://doi.org/10.1039/c2cs15319j.

[45] R.W.G. Wyckoff, Interscience Publishers, New York, New York Rocksalt Structure, 1963.

[46] A.I. Gusev, Phase diagrams of the pseudo-binary TiC - NbC, TiC - TaC, ZrC - NbC, ZrC - TaC, and HfC - TaC carbide systems (in English), Russ. J. Phys. Chem. 59 (1985) 336–340.

[47] Y.D. Blum, H.-J. Kleebe, Chemical reactivities of hafnium and its derived boride, carbide and nitride compounds at relatively mild temperature, J. Mater. Sci. 39 (2004) 6023–6042, https://doi.org/10.1023/B:JMSC.0000041699.31019.03.

[48] J. Suri, L.L. Shaw, M.F. Zawrah, Tailoring the relative Si_3N_4 and SiC contents in Si_3N_4/SiC nanopowders through carbothermic reduction and nitridation of silica fume, Int. J. Appl. Ceram. Technol. 9 (2012) 291–303, https://doi.org/10.1111/j.1744-7402.2011.02710.x.

[49] H.D. Batha, E.D. Whitney, Kinetics and mechanism of the thermal decomposition of Si_3N_4, J. Am. Ceram. Soc. 56 (1973) 365–369, https://doi.org/10.1111/j.1151-2916.1973.tb12687.x.

[50] M. Hnatko, D. Galusek, P. Šajgalík, Low-cost preparation of Si_3N_4–SiC micro/nano composites by in-situ carbothermal reduction of silica in silicon nitride matrix,

J. Eur. Ceram. Soc. 24 (2004) 189–195, https://doi.org/10.1016/S0955-2219(03)00604-6.

N. H. Wada, M.-J. Wang, T. Tien, Stability of phases in the Si-C-N-O system, J. Am. Ceram. Soc. 71 (1988) 837–840, https://doi.org/10.1111/j.1151-2916.1988.tb07532.x.

O. C. Vakifahmetoglu, E. Pippel, J. Woltersdorf, P. Colombo, Growth of one-dimensional nanostructures in porous polymer-derived ceramics by catalyst-assisted pyrolysis. Part I: Iron catalyst, J. Am. Ceram. Soc. 93 (2010) 959–968, https://doi.org/10.1111/j.1551-2916.2009.03448.x.

P. G. Gregori, H.-J. Kleebe, D.W. Readey, G.D. Soraru, Energy-filtered TEM study of Ostwald ripening of Si nanocrystals in a SiOC glass, J. Am. Ceram. Soc. 89 (2006) 1699–1703, https://doi.org/10.1111/j.1551-2916.2006.00971.x.

[54] H.-J. Kleebe, D. Suttor, H. Müller, G. Ziegler, Decomposition-crystallization of polymer-derived Si-C-N ceramics, J. Am. Ceram. Soc. 81 (1998) 2971–2977, https://doi.org/10.1111/j.1151-2916.1998.tb02722.x.

[55] R. Anand, B.B. Nayak, S.K. Behera, Coarsening kinetics of nanostructured ZrO_2 in Zr-doped SiCN ceramic hybrids, J. Alloy. Compd. 811 (2019), 151939, https://doi.org/10.1016/j.jallcom.2019.151939.

[56] H. Schmidt, W. Gruber, G. Borchardt, P. Gerstel, A. Müller, N. Bunjes, Coarsening of nano-crystalline SiC in amorphous Si–B–C–N, J. Eur. Ceram. Soc. 25 (2005) 227–231, https://doi.org/10.1016/j.jeurceramsoc.2004.08.004.

[57] R. Sujith, A.B. Kousaalya, R. Kumar, Coarsening induced phase transformation of Hafnia in polymer-derived Si-Hf-C-N-O ceramics, J. Am. Ceram. Soc. 94 (2011) 2788–2791, https://doi.org/10.1111/j.1551-2916.2011.04719.x.